

# Abundance anomalies in pre–main-sequence stars

## Stellar evolution models with mass loss

M. Vick<sup>1,3</sup>, G. Michaud<sup>2,3</sup>, J. Richer<sup>3</sup>, and O. Richard<sup>1</sup>

<sup>1</sup> GRAAL UMR5024, Université Montpellier II, CC072, Place E. Bataillon, 34095 Montpellier Cedex 05, France

<sup>2</sup> LUTH, Observatoire de Paris, CNRS, Université Paris Diderot, 5 Place Jules Janssen, 92190 Meudon, France

<sup>3</sup> Département de physique, Université de Montréal, Montréal, Québec, H3C 3J7, Canada  
e-mail: mathieu.vick@umontreal.ca, michaudg@astro.umontreal.ca,  
jacques.richer@umontreal.ca, olivier.richard@graal.univ-montp2.fr

Received August 5th, 2010; Accepted October 10th, 2010

### ABSTRACT

**Aims.** The effects of atomic diffusion on internal and surface abundances of A and F pre–main-sequence stars with mass loss are studied in order to determine at what age the effects materialize, as well as to further understand the processes at play in HAeBe and young ApBp stars.

**Methods.** Self-consistent stellar evolution models of 1.5 to 2.8  $M_{\odot}$  with atomic diffusion (including radiative accelerations) for all species within the OPAL opacity database were computed and compared to observations of HAeBe stars.

**Results.** Atomic diffusion in the presence of weak mass loss can explain the observed abundance anomalies of pre–main-sequence stars, as well as the presence of binary systems with metal rich primaries and chemically normal secondaries such as V380 Ori and HD72106. This is in contrast to turbulence models which do not allow for abundance anomalies to develop on the pre–main-sequence. The age at which anomalies can appear depends on stellar mass.

**Conclusions.** For A and F stars, the effects of atomic diffusion can modify both the internal and surface abundances before the onset of the main-sequence. The appearance of important surface abundance anomalies on the pre–main-sequence does not require mass loss, though the mass loss rate affects their amplitude. Observational tests are suggested to decipher the effects of mass loss from those of turbulent mixing. If abundance anomalies are confirmed in pre–main-sequence stars they would severely limit the role of turbulence in these stars.

**Key words.** Diffusion — stars: chemically peculiar — stars: mass-loss — stars: pre–main-sequence — stars: evolution — stars: abundances

## 1. Astrophysical context

The recent availability of magnetic field data from instruments such as ESPaDOnS at the Canada-France-Hawaii Telescope and Narval at the Bernard Lyot Telescope has allowed stellar physicists to explore long standing questions in stellar physics. A flurry of recent studies have specifically focused on observing globally organized magnetic fields in intermediate mass pre–main-sequence (PMS) stars in order to determine the origin of magnetic fields in the chemically peculiar Ap/Bp stars (Donati et al., 1997; Alecian et al., 2005; Wade et al., 2005; Catala et al., 2007; Alecian et al., 2008a,b; Folsom et al., 2008; Alecian et al., 2009). This is particularly interesting since A and B type stars have, at most, a very thin convective envelope, which is probably not sufficient to generate solar type, dynamo driven, magnetic fields. With this in mind, the favored hypothesis used to explain the presence of important magnetic fields (from 100 G to 10 kG) in A and B main-sequence (MS) stars is the fossil field theory. In this context, the magnetic field would either have originated in the molecular cloud from which the star was born, or would have been generated by a dynamo process in the core during the star’s earliest evolutionary stages. To test this hypothesis, the above mentioned studies have concentrated their efforts on characterizing magnetic fields in Herbig (HAeBe) stars (Herbig, 1960), which are believed to be the PMS progenitors of Ap/Bp stars (Wade et al., 2005).

In some cases, namely for HD72106, RS Cha and V380 Ori, binarity allows us to probe the effects of chemical separation since both stars likely had the same initial composition. In fact, for at least two of these systems, the secondary has a solar metallicity, whereas the heavier primary star has an above solar metallicity and is likely chemically anomalous. Since atomic diffusion timescales generally decrease when stellar mass increases, chemical separation could perhaps offer an explanation.

Furthermore, a more thorough analysis may allow to characterize other phenomena at play within these stars. What can the observed abundances tell us on the various processes, such as convection, mass loss and magnetic fields, which compete with atomic diffusion? And on what timescales can we expect significant surface abundance anomalies? This paper will address both of these questions.

In Vick et al. (2010) (hereafter Paper I), stellar evolution models with mass loss were introduced and shown to reproduce observed surface abundance anomalies for many AmFm stars. However, observed abundance anomalies do not allow to determine whether it is mass loss or turbulence which is competing with atomic diffusion within the radiative zone of these stars. It was nonetheless established that the surface anomalies of AmFm stars were modulated by chemical separation which occurs deep within the star. Indeed, for both the mass loss models and models with turbulent mixing (Richer et al., 2000; Richard et al., 2001, and references therein), chemical separation near  $\log \Delta M/M_{*} \approx$

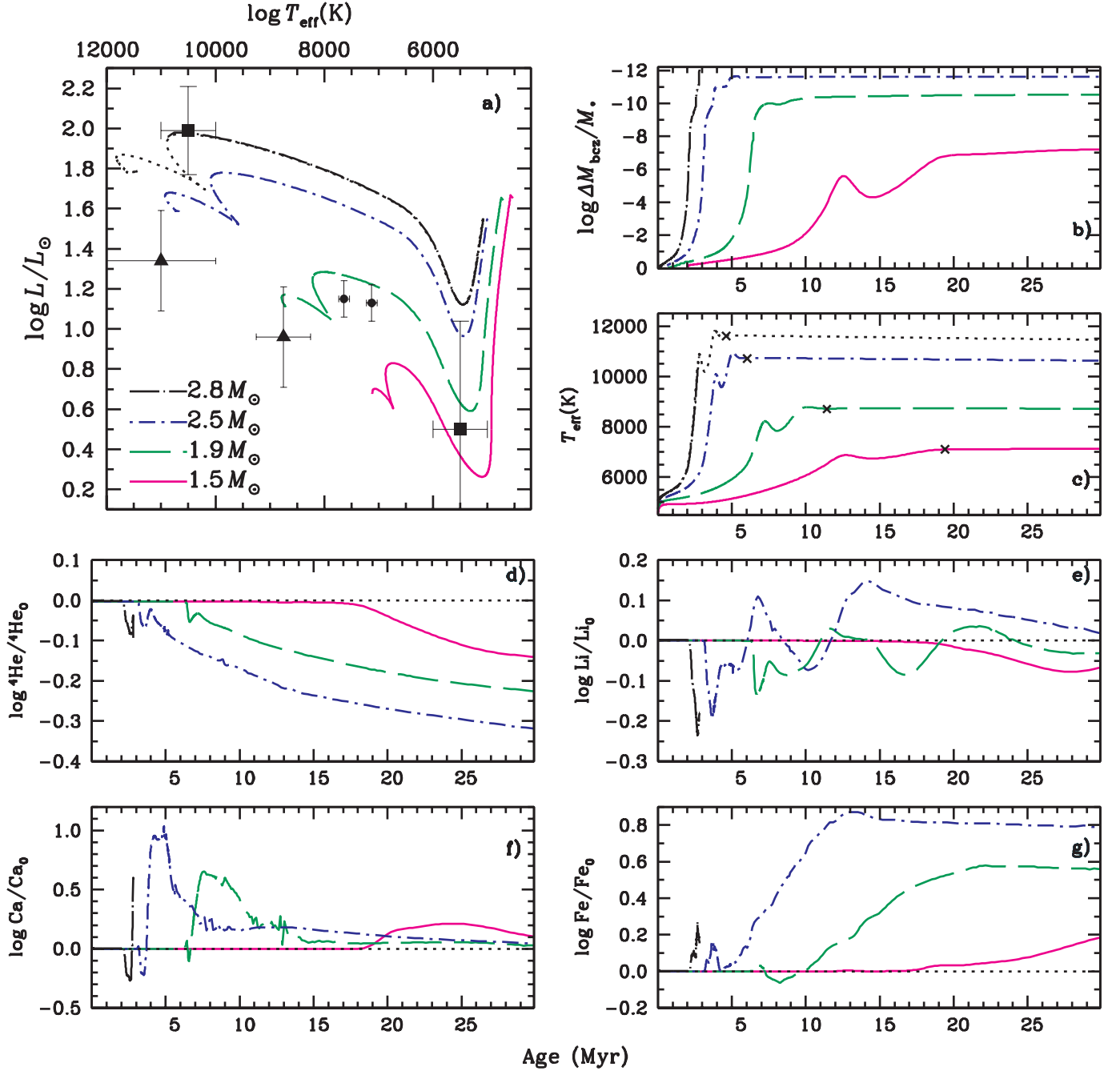


**Fig. 1.** The position in the HR diagram (a) is shown for four models with a mass loss rate of  $5 \times 10^{-14} M_{\odot} \text{yr}^{-1}$ . The curves end (on the left) at 30 Myr, age at which all the models are on the main-sequence. The dotted segment of the  $2.80 M_{\odot}$  curve represents a model with a mass loss rate of  $10^{-13} M_{\odot} \text{yr}^{-1}$  and was added in (a) and (c) in order to facilitate extrapolation, though it was not added in other panels for which the mass loss rate has an effect. Observations are shown in the HR diagram for three sets of binary stars: ( $\blacksquare$ ) V380 Ori (Alecian et al. 2009); ( $\blacktriangle$ ) HD72106 (Folsom et al. 2008); ( $\bullet$ ) RS Cha (Alecian et al. 2005). The evolution of the bottom of the surface convection zone (b),  $T_{\text{eff}}$  (c), as well as the abundances of He (d),  ${}^7\text{Li}$  (e), Ca (f) and Fe (g) are also shown. In panel (c), (x) marks the approximate end of the PMS.

–5 to –6 is responsible for the anomalous surface behavior. For PMS stars on the other hand, chemical separation which occurs at this depth cannot explain observed abundance anomalies since the timescales are much too long. In mass loss models, chemical separation occurring near the surface leads to anomalies which

appear at the surface within a few Myr, and could therefore reconcile observations.

In the following analysis, and in our calculations, mass loss is considered in *non rotating* stars, since in such stars, mass loss could be the only process competing with atomic diffusion within the stable radiative zones. An outline of the main aspects

of our evolution code is found in Sect. 2. The stellar models will be presented in Sect. 3, with particular attention to the various effects of mass loss and atomic diffusion in the interior (Sect. 3.1) and at the surface (Sect. 3.2) of PMS stars. In Sect. 4, the models are compared to observations of various HAeBe stars. Finally, in Sect. 5, the implications of our results on the processes involved in HAeBe and, by extension, in ApBp stars will be discussed.

## 2. Calculations

The detailed description of the stellar evolution code used for these computations can be found in Paper I and references therein. At age zero, all models are fully convective with the abundance mix prescribed in Table 1 of Turcotte et al. (1998). Opacities are continuously updated for every mesh point as abundances evolve. The only adjustable parameter, the mixing length parameter  $\alpha$ , was calibrated by fitting the current radius and luminosity of the Sun (see model H of Turcotte et al. 1998). Radiative accelerations are taken from Richer et al. (1998) with corrections due to redistribution from Gonzalez et al. (1995) and LeBlanc et al. (2000). The introduction of mass loss and its impact on transport are discussed extensively in Sect. 4 of Paper I.

No extra mixing is enforced outside of convection zones. The effects of atomic diffusion materialize as soon as radiative zones appear as the models evolve toward the MS. These effects become more important as the radiative zone expands toward the surface, where atomic diffusion timescales are much shorter.

The unseparated<sup>1</sup> mass loss rates considered range from  $10^{-14}$  to  $10^{-13} M_{\odot} \text{yr}^{-1}$ : mass loss rates which lead to surface abundances compatible with observations of many AmFm stars. Due to uncertainties related to the nature of winds for A and F stars (see discussion in Sect. 4.2 of Paper I), we have chosen to limit our investigation to unseparated winds in order to avoid introducing additional adjustable parameters.

Finally, this paper is part of a series of papers starting with Turcotte et al. (1998), where the mixing length used was calibrated using the Sun for given boundary conditions, helium and metal abundances. For consistency, and in order to isolate the effects of the processes of interest, the same boundary condition, solar composition and mixing length are used for all calculations of Pop I stars (see also Sect. 2 of Paper I).

## 3. Evolutionary models

In Fig. 1, the position in the Hertzsprung–Russell (HR) diagram, the evolution of  $\Delta M_{\text{BSCZ}}^2$ ,  $T_{\text{eff}}$  as well as of the surface abundances of He,  $^7\text{Li}$ , Ca and Fe are shown for four stellar models with the same mass loss rate ( $5 \times 10^{-14} M_{\odot} \text{yr}^{-1}$ ). Due to numerical instabilities related to the complete disappearance of the surface convection zone, the 2.80W5E-14<sup>3</sup> model could not be converged up to the main-sequence. Therefore, in order to complete the HR diagram, the curve was continued using a 2.80W1E-13 model. In this case, the effect of doubling the mass loss rate on the position in the HR diagram is smaller than the width of the line. Its effect on surface abundances will be discussed in Sect. 3.2.

The exact definition of the MS and, by extension, the PMS is somewhat arbitrary. The definition given by Iben (1965) stipulates that the *zero age* main-sequence (ZAMS) begins when the

thermal-gravitational energy is reduced to one percent of the luminosity of the star, although this may depend on such things as the treatment of convection (Cox, 1968). According to this definition, immediately after the end of the PMS, indicated by a (x) in Fig. 1c,  $T_{\text{eff}}$  and  $L$  begin varying much more slowly. The time spent on the PMS varies from  $\sim 4$  Myr for the 2.80W5E-14 model to  $\sim 19$  Myr for the 1.50W5E-14 model.

### 3.1. Radiative accelerations, internal abundances and structure

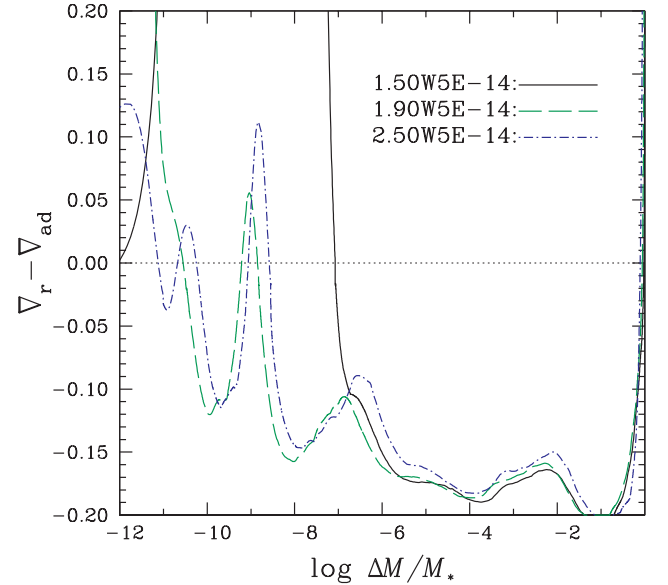


**Fig. 2.** Internal variation of  $\nabla_r - \nabla_{ad}$  for three models with a mass loss rate of  $5 \times 10^{-14} M_{\odot} \text{yr}^{-1}$  at the onset of the ZAMS. The surface is at  $\log \Delta M / M_* = -12$  and transport is convective when  $\nabla_r - \nabla_{ad} > 0$ . For different masses, the position of convection zones in relation to  $\log \Delta M / M_*$  changes slightly, though it is constant in relation to  $T$ .

Even on the PMS, the internal structure and abundances vary significantly between  $1.5 M_{\odot}$  and  $2.8 M_{\odot}$ . In Fig. 2, convection zones are shown for models of different mass as they arrive on the ZAMS (see also Fig. 1b). The internal distribution of convection zones is strongly correlated with stellar mass. For the  $1.50 M_{\odot}$  model, the SCZ includes the linked H and He convection zones and is never shallower than  $\log \Delta M / M_* = -7.2$  (see also Fig. 1b). For the  $1.90 W5E-14$  model, the surface convection zones separate into a linked H–He I CZ and a deeper He II CZ, while a separate He I CZ materializes in the heavier  $2.50 W5E-14$  model. All convection zones disappear completely in the  $2.80 W5E-14$  model before it has even arrived on the MS (see Fig. 1b). Finally, over the entire PMS phase, the opacity bump near  $\log \Delta M / M_* \sim -7.2$  resulting from iron peak element accumulation is not large enough to induce an iron peak convection zone for any of the three models, though iron peak opacity might extend the SCZ slightly inward for the  $1.50 W5E-14$  model. If the mass loss rate is  $\leq 10^{-14} M_{\odot} \text{yr}^{-1}$ , an iron convection zone may appear after the PMS (see Fig. 5 of Paper I).

Significant abundance variations appear in the interior of our PMS models. For example, in the  $2.50 W5E-14$  model (bottom row of Fig. 3), a 1.1 dex Ca overabundance develops at

<sup>1</sup> Having the same composition as the photosphere.

<sup>2</sup> BSCZ: bottom of surface convection zone.

<sup>3</sup> The expression 2.80W5E-14 corresponds to a  $2.80 M_{\odot}$  model with a mass loss rate of  $5 \times 10^{-14} M_{\odot} \text{yr}^{-1}$ .

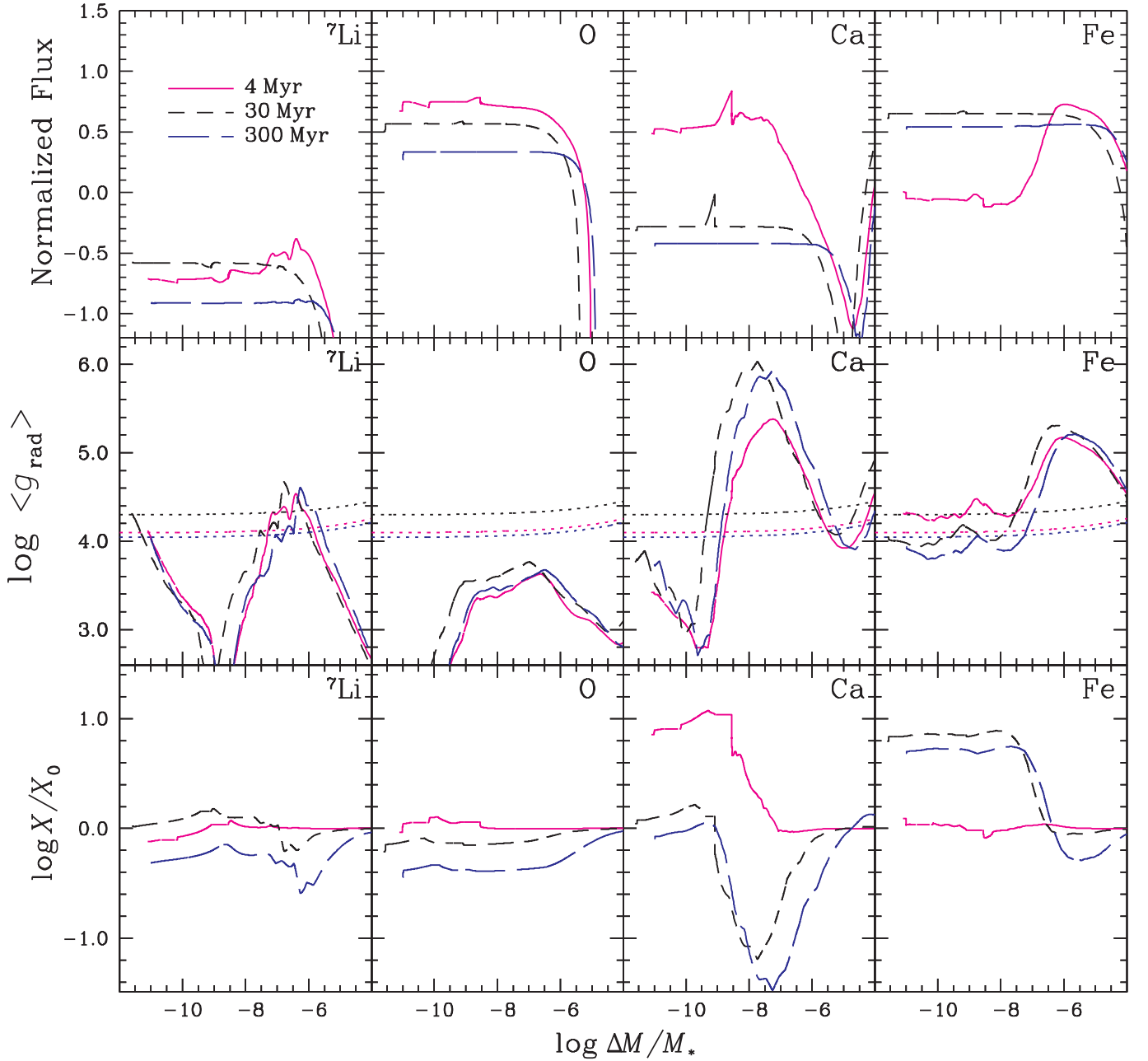


**Fig. 3.** Comparison of the normalized local flux with radiative accelerations and internal abundances of  ${}^7\text{Li}$ , O, Ca and Fe at 3 different ages for the 2.50W5E-14 model. The curves end (on the left) at the bottom of the surface convection zone. In the middle row, the dotted line represents gravity.

$\log \Delta M/M_* \simeq -9.4$  as early as 4 Myr. It might seem puzzling however that such an overabundance transforms into a strong underabundance which reaches below  $-1$  dex at 30 Myr. Why should the behavior at 4 Myr be so different from the rest of the star's evolution and why does a strong overabundance develop in a region where  $g_{\text{rad}}(\text{Ca})$  is below gravity? The reason stems from the fact that the wind progressively advects matter from deeper within the star. That depth is simply given by:

$$\Delta M \simeq \dot{M}t. \quad (1)$$

So, at 4 Myr, the wind brings to the surface matter which originates from  $4 \times 10^6 \text{ yr} \cdot 5 \times 10^{-14} \text{ M}_\odot \text{ yr}^{-1} = 2 \times 10^{-7} \text{ M}_\odot \sim 10^{-7} M_*$ .

Correspondingly, one sees in the top row of Fig. 3 that the flux is nearly constant from the surface down to that depth (except over CZs), while it is clearly not constant below that depth. Naturally, the depth above which the flux is conserved due to advection from the wind increases with age (compare the curves at 4, 30 and 300 Myr). In order to conserve the flux,  $X(\text{Ca})$  at 4 Myr increases above  $\Delta M/M_* \sim 10^{-7}$  to compensate for the decrease in  $g_{\text{rad}}(\text{Ca})$ <sup>4</sup>. This process can be described by:

$$\mathcal{F}(r) = \text{cst} \simeq r^2 \rho (U + U_w) c \quad (2)$$

<sup>4</sup> The same type of solution was obtained for oxygen in Landstreet et al. (1998).

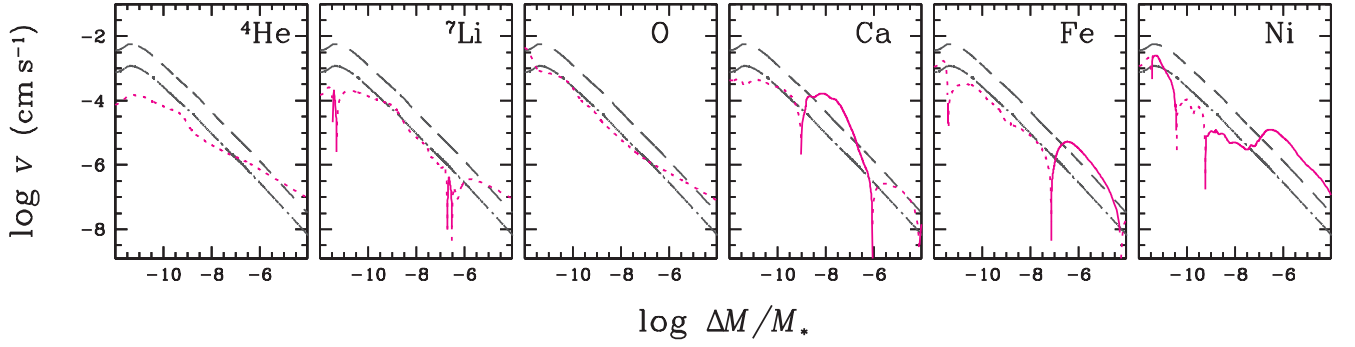


**Fig. 4.** Wind velocities (dot-dashed line:  $10^{-14} \text{ M}_{\odot}\text{yr}^{-1}$ ; dashed line:  $5 \times 10^{-14} \text{ M}_{\odot}\text{yr}^{-1}$ ) and diffusion velocities (solid when positive, toward the surface, and dotted when negative) of a few selected elements in a  $1.90 \text{ M}_{\odot}$  model near the ZAMS. For most species, wind velocities decrease more rapidly inwards than diffusion velocities.

where  $\mathcal{F}(r)$  is the local flux at radius  $r$ ,  $\rho$  is the local density,  $U$  and  $U_w$  are the advective part of the atomic diffusion velocity and wind velocity respectively, and  $c$  is concentration<sup>5</sup>. Although gravity is stronger than  $g_{\text{rad}}$  over a fraction of the stellar envelope for all elements shown in Fig. 3, the downward diffusion velocity is never larger than the wind velocity (see Fig. 4 for an example with a  $1.9 \text{ M}_{\odot}$  model). Therefore, as long as the absolute value of the wind velocity is larger than the downward diffusion velocity, any given element is dragged toward the surface, and its local abundance adjusts in order to conserve flux. Notice that the fraction of the envelope  $\Delta M$  which can be described by Eq. [2] increases with time since the wind progressively advects more mass toward the surface.

With this in mind, one can understand that at  $t = 4 \text{ Myr}$ , the increase of  $X(\text{Ca})$  above  $\Delta M/M_* \sim 10^{-7}$  is generated by the large flux arriving from regions where  $g_{\text{rad}}(\text{Ca})$  is larger than gravity and which is conserved even as  $g_{\text{rad}}(\text{Ca})$  decreases toward the surface. As time passes, Ca arrives at the surface from deeper within the star, where  $g_{\text{rad}}(\text{Ca})$  is much smaller than its value at  $\Delta M/M_* \sim 10^{-7}$ , so that the flux is smaller, the flux conservation applies over a larger mass and the surface abundance consequently decreases. This shows the importance of a solution over the whole star, as done here, since applying an inner boundary condition at  $\Delta M/M_* \sim 10^{-7}$  would lead to an erroneous solution after 4 Myr.

On the PMS, the internal concentration variations are much smaller for  ${}^7\text{Li}$ , O and Fe than for Ca. However, after the star arrives on the MS, as illustrated by the curve at 30 Myr, larger variations appear, including a nearly  $\sim 0.8$  dex overabundance of Fe which spans from the surface down to  $\log \Delta M/M_* \sim -8$ .

As shown in Fig. 4, for a mass loss rate of  $10^{-14} \text{ M}_{\odot}\text{yr}^{-1}$ , the downward diffusion velocity is greater than the wind velocity for some elements, whereby the flux conservation regime as described by Eq. [2] cannot be extended to all elements. The regime shift approximately occurs at  $2 \times 10^{-14} \text{ M}_{\odot}\text{yr}^{-1}$  (see Fig. 5 of Paper I and corresponding discussion). This mass loss rate also marks the limit below which iron accumulation near  $T \sim 200\,000 \text{ K}$  can lead to iron peak convection (see Fig. 5 of Paper I).

### 3.2. Surface abundances

An element's surface abundance depends on age, stellar mass and mass loss rate. In Fig. 1, the surface abundances of He,  ${}^7\text{Li}$ ,

Ca and Fe are shown for models of 1.5, 1.9, 2.5 and  $2.8 \text{ M}_{\odot}$  with a mass loss rate of  $5 \times 10^{-14} \text{ M}_{\odot}\text{yr}^{-1}$ . As stellar mass increases, anomalies appear at the surface earlier. For instance, at around 3 Myr the  $2.80\text{W5E-14}$  model has a 0.6 dex overabundance of Ca while all other models still have their initial abundances (Fig. 1g). The same can be said for Fe overabundances or He underabundances, which appear later in smaller stellar mass models. Nonetheless, it is evident that for a given element, the overall shape of the surface abundance evolution curve is very similar for the three heavier models. This is due to two things: the appearance of a separate He II CZ, as well as flux conservation as described in the previous section.

For all four elements shown in Fig. 1, the initial, short-lived abundance maxima are caused by evolutionary effects. The appearance of a radiative zone which separates the He II CZ from the SCZ allows for chemical separation to occur near the surface. The direction of the anomaly is determined by  $g_{\text{rad}}-g$  within that region (between  $\log \Delta M/M_* \sim -10.5$  and  $-9$ ), and thus He,  ${}^7\text{Li}$  and Ca become underabundant, whereas Fe develops an overabundance (compare middle panel of Fig. 3 with Fig. 1). Following this brief episode, the surface abundance is determined by flux conservation, and so results from chemical separation occurring deeper within the star<sup>6</sup>. For instance, the subsequent, gradual  $X(\text{Fe})$  increase results from the wind slowly advecting matter which originated below  $\log \Delta M/M_* \sim -7$  (for the  $2.50\text{W5E-14}$  model), where  $g_{\text{rad}}(\text{Fe})$  is greater than  $g$ . Similarly, the variations of  $X({}^7\text{Li})$  which materialize at the surface are due to variations seen in  $g_{\text{rad}}({}^7\text{Li})$  between  $\log \Delta M/M_* \sim -7.5$  and  $-6$ .

The amplitude of the anomalies also depends on stellar mass. The Ca overabundance that materializes on the PMS in the three heavier models reaches 0.65 dex for the  $1.90\text{W5E-14}$  model, while it reaches 1.1 dex in the  $2.50\text{W5E-14}$  model. The He and  ${}^7\text{Li}$  underabundances, as well as the initial Fe overabundance follow the same dependence. The  $1.50\text{W5E-14}$  model behaves differently since most of the mass interval from  $\log \Delta M/M_* \sim -7.5$  and  $-6$  is mixed by convection (see Fig. 2).

<sup>6</sup> Thermohaline convection, as described in Théado et al. (2009), should not affect our results as the small mean molecular weight gradients that materialize occur in or just below the He II CZ, and should not affect surface abundances — after a fraction of a Myr (see Sect. 3.1) — if the internal solution is dominated by the wind (e.g.  $\dot{M} \gtrsim 2 \times 10^{-14}$ , see also Fig. 9 and discussion in Sect. 8.1 of Paper I).

<sup>5</sup> This equation is derived and discussed in Sect. 5.1.1 of Paper I.



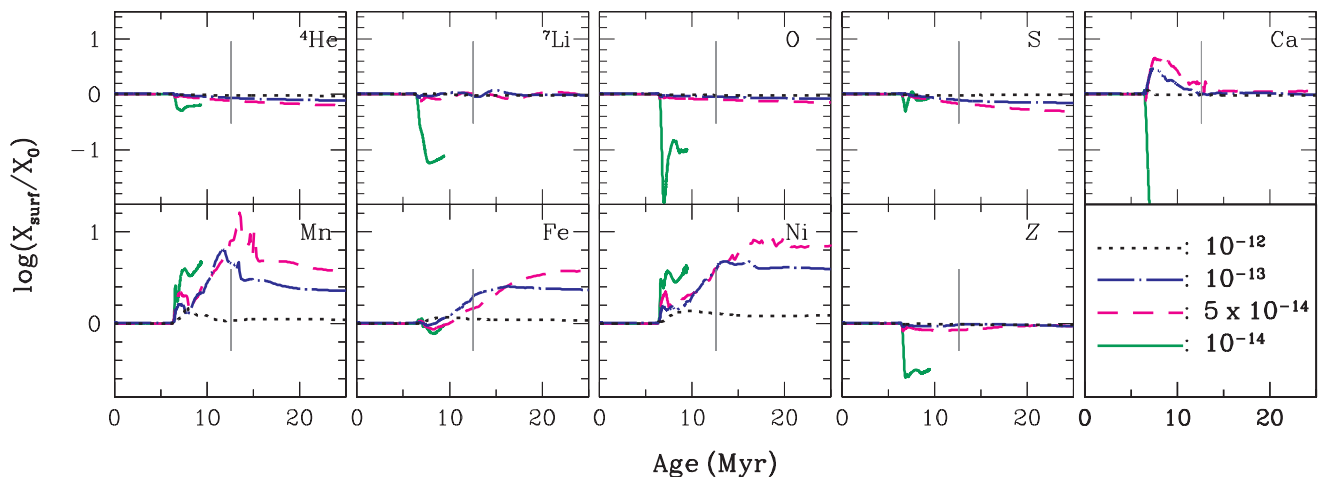


**Fig. 5.** Surface abundance variations for models of  $1.9 M_{\odot}$  with different mass loss rates which are identified in the lower right panel in  $M_{\odot}\text{yr}^{-1}$ . The vertical line indicates the approximate end of the PMS.

### 3.2.1. Effect of varying the mass loss rate

Generally, increasing the mass loss rate lowers the amplitude of surface abundance anomaly extrema, as sinking elements are further advected toward the surface while supported elements are more effectively evacuated. In Fig. 5, the surface abundances are shown for a  $1.9 M_{\odot}$  model with four different mass loss rates. For this model, the PMS ends near 10 Myr (see Fig. 1c). For the  $1.90W5E-14$  and  $1.90W1E-13$  models, He, O and S decrease slowly and monotonically, while Li oscillates around its initial value. A calcium overabundance occurs at  $\sim 7$  Myr, after which  $X(\text{Ca})$  returns to its original value near the end of the PMS. Iron peak elements are overabundant for both models throughout the PMS and onto the MS, with Fe maxima of 0.4 and 0.6 dex for the  $1.90W1E-13$  and  $1.90W5E-14$  models respectively. For all elements, maximum amplitudes are smaller when the mass loss rate is larger.

The  $1.90W1E-14$  behaves quite differently: large anomalies appear very rapidly, especially for sinking elements;  ${}^7\text{Li}$  and O underabundances reach  $-1.2$  and  $-2$  dex respectively, while Ca is more than 100 times underabundant as soon as chemical separation reaches the surface. This is because, in contrast to the other two mass loss rates, the wind generated by a mass loss rate of  $10^{-14} M_{\odot}\text{yr}^{-1}$  is not strong enough to dominate inward diffusion for most sinking elements. In Fig. 4, for instance, one can see that for this mass loss rate, the inward diffusion velocity of  ${}^7\text{Li}$ , O and Ca is greater or equal to the wind velocity over an important fraction of the upper layers. On the other hand, supported elements behave as in the other two models, though with larger overabundances (at least up to the age of the last converged model). This is logical since the weaker wind cannot evacuate as much of the metal rich material which has accumulated in the SCZ.

On the PMS, and for this stellar mass, only the  $1.90W1E-14$  model generates sufficient anomalies to cause Z to vary significantly from its original value. The  $1.90W1E-12$  model only allows very small abundance anomalies at the surface ( $\sim 0.1$  dex).

### 3.2.2. Comparison to turbulence models

In the models of Richer et al. (2000), turbulent mixing down to  $T \sim 200\,000$  K, the depth of the iron peak CZ, is assumed to be

the process which competes with atomic diffusion in the stellar interior. However, due to efficient mixing, abundance anomalies do not appear at the surface of these models until they have arrived on the MS. The significant overabundance of Ca in mass loss models (Fig. 1f, see also Alecian 1996), is not obtained in the above mentioned models with turbulence, and so could be used as an observational test for young stars.

## 4. Comparison to observations

Confronting our models to observations can offer constraints on mass loss rates as well as on mixing processes near the surface, such as convection. However, in order to compare models with observations, one must try to fit various parameters simultaneously, including age, mass (or  $T_{\text{eff}}$ ) and initial surface composition. To reduce the arbitrariness of the comparison, we chose three binary systems, since both components of such systems should have the same age and initial abundances. Unfortunately, determining this age and initial abundance mix is difficult. For all three systems, the age deduced by observers was determined using model isochrones in which many assumptions were necessary. For instance, in all three cases atomic diffusion was neglected, and large mass loss or accretion rates ( $\sim 10^{-8} M_{\odot}\text{yr}^{-1}$ ) were assumed. For this reason, we believe that it is preferable to fit the position in the HR diagram from this study rather than use the age determined by other isochrones. As for initial abundances, two of the systems have a chemically “normal” secondary which offers a glimpse into the initial metal content, even though “normal” abundances can mean different things depending on the solar mix used as a reference<sup>7</sup>. However, assuming that both components of a given binary system have the same initial abundances allows us to make a differential comparison of surface abundances and conclude that differences between the two are caused by internal processes such as atomic diffusion. The chosen original abundances aren’t crucial for our analysis since our objective here is to show *when* abundance anomalies appear on the PMS, which is not very sensitive to the ini-

<sup>7</sup> There is still much debate on the newer Asplund et al. (2005) and Asplund et al. (2009) initial solar abundance mix for which abundances of CNO are significantly lower than the older solar mix of Grevesse et al. (1996); the latter are in better agreement with helioseismology models (Delahaye & Pinsonneault 2006).

tial abundances used to construct the models (see Fig. 13 and Sect. 8.1 of Paper I).

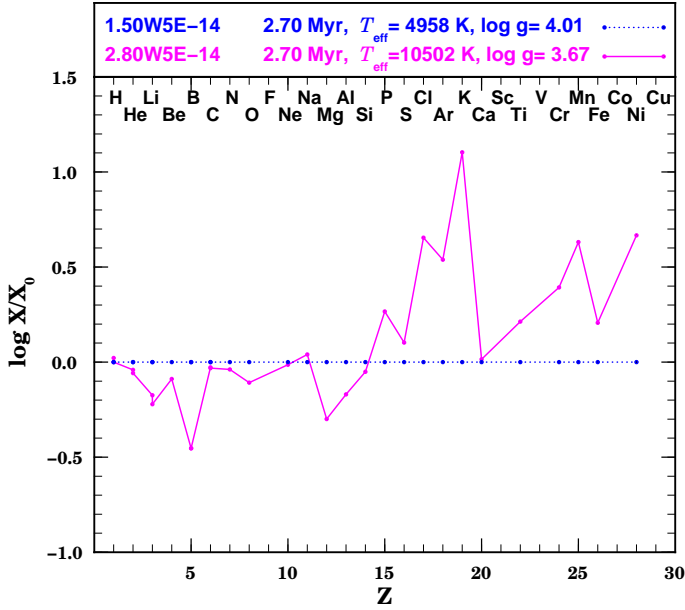


**Fig. 6.** Surface abundances for models representing the components of the binary star V380 Ori. The models were chosen at the age which best fits the primary in the HR diagram (Fig. 1a). In both models, the mass loss rate is  $5 \times 10^{-14} M_{\odot} \text{yr}^{-1}$ .

In Fig. 1, models are compared to three observed binary systems: V380 Ori (■), HD72106 (▲) and RS Cha (●), which are all believed to be HAeBe stars. For the Ae star V380 Ori (Alecian et al. 2009), the  $2.87 M_{\odot}$  primary and  $1.6 M_{\odot}$  chemically normal secondary are compared to the 2.80W5E-14 and 1.50W5E-14 models respectively. Within the error bars, the fit in the HR diagram is very good and the corresponding age of the primary is  $\sim 2.7$  Myr (the age given in Alecian et al. 2009 is  $2 \pm 1$  Myr). The 2.80W5E-14 model has developed overabundances of Fe and Ca which reach  $\sim 0.3$  dex and  $\sim 0.6$  dex respectively. Though this model could only be converged until 2.8 Myr, it has already developed anomalies which explain the high metallicity ( $[M/H]=0.5$ ) determined in Alecian et al. (2009). As illustrated in Fig. 6, most metals heavier than  $Z \geq 15$  are overabundant by a factor of  $\sim 2-3$ , while CNO are barely underabundant. Lithium becomes  $-0.2$  dex underabundant. At the best fitting age for the primary, the 1.50W5E-14 model still has its initial abundances, which also agrees with observations. The potential effect of a magnetic field, which is observed in the primary, will be discussed in Sect. 5.

For HD 72106, the  $2.4 M_{\odot}$  primary and the  $1.9 M_{\odot}$  secondary are compared to the 2.50W5E-14 and 1.90W5E-14 models respectively. In the HR diagram, the fit is not perfect, especially for the primary, though this was also problematic in Fig. 4 of Folsom et al. (2008). In fact, these authors suggest that at a determined age of 6–13 Myr (our best fit model is between 5–7 Myr), the primary is most likely on the ZAMS rather than the PMS. Nonetheless, they found that the primary was chemically anomalous with important overabundances of iron peak elements and a strong underabundance of He, while the secondary is almost solar. In the best fitting models for the primary (5–7 Myr), iron

overabundances vary from about 0.1 to 0.3 dex, while Ca overabundances vary from about 1 dex down to about 0.3 dex. For the same age interval, the He underabundance varies from  $-0.1$  to  $-0.15$  dex. These amplitudes are smaller than the observed values. This could be due to the mass loss rate being too large (see Fig. 5). The presence of a magnetic field and of phase variations (see Fig. 9 of Folsom et al. 2008) do not justify trying to achieve a better fit. A precise model would require 2 or 3 D calculations. Furthermore, some uncertainty remains on the exact amplitudes since all their abundances were determined simultaneously by fitting the observed spectra for a single averaged phase. Over this same age interval, the secondary still has its initial abundances, which agrees with observations.

For RS Cha, the  $1.89 M_{\odot}$  primary and the  $1.87 M_{\odot}$  secondary may be compared to the 1.90W5E-14 model. In the HR diagram, the slight discrepancy with the model can be explained by the slight difference in stellar mass. Within reasonable error bars, the model is either chemically normal (up to 6.7 Myr), or has developed an overabundance of Ca of about 0.4 dex accompanied by small underabundances of  $^7\text{Li}$  and He of  $-0.11$  dex and  $-0.05$  dex respectively. This model does not seem to explain the iron enrichment factor of 1.5 obtained by the authors. However, in contrast to the two previous binary systems, both these stars have the same composition; therefore, there is no difference in composition between the stars to explain, and so the initial abundances could be responsible for the abundance anomalies with respect to the solar composition. The X-ray emission observations of Mamajek et al. (1999) suggest that accretion could play a role. A smaller mass loss rate would also lead to larger anomalies.

Other young single HAeBe stars which are not shown in Fig. 1 may also be compared to our models. The star HD 104237 has a mass of about  $2.3 M_{\odot}$  ( $T_{\text{eff}} = 8000$  K), a luminosity of about  $1.42 L_{\odot}$  (Böhm et al. 2004) and an approximate age of 2 Myr (van den Ancker et al. 1998), as well as a magnetic field of about 50 G (Donati et al., 1997, 2000). It is an HAeBe star for which Acke & Waelkens (2004) found that Si, Cr and Fe abundances were solar, which agrees with our results since even the heavier 2.50W5E-14 model is roughly normal until 3 Myr (see Fig. 1). Similarly, HD 190073, which has an age of  $1.2 \pm 0.6$  Myr and a mass of  $2.85 \pm 0.25 M_{\odot}$  ( $T_{\text{eff}} = 9250$  K), was also found to be roughly solar (Acke & Waelkens 2004). Within the timescales shown in Fig. 1, this is also compatible with our results. Finally, though it has just recently embarked on the MS, the young magnetic Bp cluster star NGC 2244-344 which has  $T_{\text{eff}} \approx 15000$  K and an age of 2 Myr (Bagnulo et al. 2004) can also be compared to our results. A rough extrapolation suggests that the observed  $\sim 1$  dex overabundances of Si and Fe and  $\sim 2$  dex overabundances of Ti and Cr, as well as the  $\sim 1$  dex underabundance of He could simply be the result of chemical separation which began on the PMS.

## 5. General discussion and conclusions

Though it is often assumed negligible for A and F type PMS stars, chemical separation resulting from atomic diffusion can affect both the surface and interior of these young stars. The mass in convection zones (Fig. 2) and internal concentrations (Fig. 3) can be modified *before* stars arrive on the MS. The amplitude of the internal concentration variations depends on stellar mass. Equivalently, the age at which abundance anomalies appear at the surface also depends on stellar mass. In the presence of weak mass loss, and for models with no turbulent mixing, rotation or magnetic fields, significant internal variations and sur-

face anomalies (both exceeding factors of 10 for some elements) appear as early as  $\sim 2$  Myr in early-type A stars, and  $\sim 20$ -25 Myr in cooler F stars.

Mass loss only slightly affects the age at which abundance anomalies occur at the surface, although its inclusion in our calculations was necessary in order to evolve models to ages of interest. This being said, mass loss does affect the maximum amplitude of surface anomalies (see Fig. 5); a mass loss rate  $\geq 10^{-12} M_{\odot} \text{yr}^{-1}$  nearly flattens surface abundance anomalies, whereas mass loss rates  $\leq 10^{-14} M_{\odot} \text{yr}^{-1}$  allow strong under-abundances of elements which are not supported by the radiation field, and may allow the appearance of an iron peak CZ.

The important Ca overabundance materializing in our models of PMS stars, which is not obtained in similar models with turbulence, could help distinguish between these two scenarios (see Sect. 3.2.2). If abundance anomalies observed at the surface of A and F type PMS stars are in fact due to chemical separation, this strongly favors the mass loss model as presented in this paper and should be confirmed by asteroseismology (see also Sect. 6 of Paper I). More precise determinations of individual elemental abundances may also allow further differentiation.

Atomic diffusion coupled with a mass loss rate which is compatible with observations of AmFm stars may elucidate why there are PMS binary systems such as V380 Ori and HD72106 for which the primary is chemically anomalous while the secondary remains roughly normal (see Sect. 4). Since diffusion timescales vary more rapidly with stellar mass than with mass loss rate (compare Figs. 1 and 5), smaller mass loss rates (or atomic diffusion on its own) may also explain these systems. Observed abundance anomalies in other single PMS stars and young ApBp stars may also result from atomic diffusion (Sect. 4), without the need for other more exotic explanations. This being said, many PMS stars have observed magnetic fields, strong accretion rates (from stellar disks) or both. These phenomena could also have an effect on transport in the external regions of the star.

A magnetic field can impact chemical transport through its effects on rotation via magnetic braking, by modifying convection in the atmosphere (Cattaneo et al. 2003), as well as by affecting atomic diffusion velocities (Alecian & Stift 2006). In single stars for which rotation cannot be slowed by tidal forces, strong magnetic fields may be the only process which sufficiently reduces rotation to allow chemical separation. Although it has to our knowledge never been shown that magnetic fields can completely eliminate convection, their topologies can induce horizontally dependent convection and abundance profiles (Babel & Michaud 1991), in addition to anisotropic mass loss and/or accretion (Théado et al. 2005). If mass loss is in fact anisotropic, then strong mass loss rates, as suggested for young PMS stars by Boehm & Catala 1995, may be present only where field lines are vertical, and thus be compatible with anisotropic surface anomalies. Similarly, magnetic fields may extend the upper limit of  $v_{\text{eq}} = 100 \text{ km s}^{-1}$ , which was found to eliminate the effects of atomic diffusion (Charbonneau & Michaud 1988). This may allow anomalies to develop even in the fast rotators among HAeBe stars (Davis et al. 1983).

However, until these processes are better understood, and magnetic field geometries are better constrained for individual stars, it would be ill-advised to introduce additional magnetic field related parameters into our calculations. The effects of magnetic fields on chemical transport may best be grasped through comparative mapping of superficial magnetic fields and abundances as done for roAp stars in Kochukhov & Wade

(2010) and Lüftinger et al. (2010), as well as for HAeBe stars in Folsom et al. (2008).

Accretion also affects elemental distribution in the atmospheres of stars. For accretion rates greater than approximately  $10^{-12} M_{\odot} \text{yr}^{-1}$ , the abundance profiles in the atmosphere, and in the interior, simply reflect those of the accreted material (Turcotte & Charbonneau 1993). For accretion rates a few times larger than  $10^{-14} M_{\odot} \text{yr}^{-1}$ , the atmospheric abundances can preserve the accreted material signature while allowing for abundance gradients due to chemical separation to develop below the SCZ. For even smaller rates, atmospheric abundances essentially reflect the result of chemical separation as if there were no accretion. In any case, as soon as the star stops accreting, chemical separation resulting from atomic diffusion dominates within 1 Myr.

In terms of stellar modelling, HAeBe stars are extremely complex: stellar winds, accretion, rotation and magnetic fields complicate simulations. Current models cannot account for all these processes without invoking multiple parameters which may blur any actual physics taking place within these stars. Though there are other processes involved, it is shown that atomic diffusion can lead to abundance anomalies on the PMS, and that neglecting its effects could have an impact on calibrating atmosphere models.

*Acknowledgements.* M. Vick would like to thank E. Alecian and C. Folsom for some very insightful discussions. He also thanks the Département de physique de l'Université de Montréal for financial support, as well as everyone at the GRAAL in Montpellier for their amazing hospitality. We acknowledge the financial support of Programme National de Physique Stellaire (PNPS) of CNRS/INSU, France. This research was partially supported by NSERC at the Université de Montréal. Finally, we thank the Réseau québécois de calcul de haute performance (RQCHP) for providing us with the computational resources required for this work.



## References

- Acke, B. & Waelkens, C. 2004, *A&A*, 427, 1009
- Alecian, E., Catala, C., van't Veer-Menneret, C., Goupil, M., & Balona, L. 2005, *A&A*, 442, 993
- Alecian, E., Catala, C., Wade, G. A., et al. 2008a, *MNRAS*, 385, 391
- Alecian, E., Wade, G. A., Catala, C., et al. 2008b, *A&A*, 481, L99
- Alecian, E., Wade, G. A., Catala, C., et al. 2009, *MNRAS*, 400, 354
- Alecian, G. 1996, *A&A*, 310, 872
- Alecian, G. & Stift, M. J. 2006, *A&A*, 454, 571
- Asplund, M., Grevesse, N., & Sauval, A. J. 2005, in *Astronomical Society of the Pacific Conference Series*, Vol. 336, *Cosmic Abundances as Records of Stellar Evolution and Nucleosynthesis*, ed. T. G. Barnes, III & F. N. Bash, 25
- Asplund, M., Grevesse, N., Sauval, A. J., & Scott, P. 2009, *ARA&A*, 47, 481
- Babel, J. & Michaud, G. 1991, *ApJ*, 366, 560
- Bagnulo, S., Hensberge, H., Landstreet, J. D., Szeifert, T., & Wade, G. A. 2004, *A&A*, 416, 1149
- Boehm, T. & Catala, C. 1995, *A&A*, 301, 155
- Böhm, T., Catala, C., Balona, L., & Carter, B. 2004, *A&A*, 427, 907
- Catala, C., Alecian, E., Donati, J., et al. 2007, *A&A*, 462, 293
- Cattaneo, F., Emonet, T., & Weiss, N. 2003, *ApJ*, 588, 1183
- Charbonneau, P. & Michaud, G. 1988, *ApJ*, 327, 809
- Cox, J. P. 1968, *Principles of stellar structure - Vol.1: Physical principles; Vol.2: Applications to stars* (New York: Gordon and Breach, 1968)
- Davis, R., Strom, K. M., & Strom, S. E. 1983, *AJ*, 88, 1644
- Delahaye, F. & Pinsonneault, M. H. 2006, *ApJ*, 649, 529
- Donati, J., Mengel, M., Carter, B. D., et al. 2000, *MNRAS*, 316, 699
- Donati, J., Semel, M., Carter, B. D., Rees, D. E., & Collier Cameron, A. 1997, *MNRAS*, 291, 658
- Folsom, C. P., Wade, G. A., Kochukhov, O., et al. 2008, *MNRAS*, 391, 901
- Gonzalez, J.-F., LeBlanc, F., Artru, M.-C., & Michaud, G. 1995, *ApJ*, 297, 223
- Grevesse, N., Noels, A., & Sauval, A. J. 1996, in *Astronomical Society of the Pacific Conference Series*, Vol. 99, *Cosmic Abundances*, ed. S. S. Holt & G. Sonneborn, 117
- Herbig, G. H. 1960, *ApJS*, 4, 337
- Iben, Jr., I. 1965, *ApJ*, 141, 993
- Kochukhov, O. & Wade, G. A. 2010, *A&A*, 513, A13+
- Landstreet, J. D., Dolez, N., & Vauclair, S. 1998, *A&A*, 333, 977
- LeBlanc, F., Michaud, G., & Richer, J. 2000, *ApJ*, 538, 876
- Lüftinger, T., Kochukhov, O., Ryabchikova, T., et al. 2010, *A&A*, 509, A71+
- Mamajek, E. E., Lawson, W. A., & Feigelson, E. D. 1999, *ApJ*, 516, L77
- Richard, O., Michaud, G., & Richer, J. 2001, *ApJ*, 558, 377
- Richer, J., Michaud, G., Rogers, F., Turcotte, S., & Iglesias, C. A. 1998, *ApJ*, 492, 833
- Richer, J., Michaud, G., & Turcotte, S. 2000, *ApJ*, 529, 338
- Théado, S., Vauclair, S., Alecian, G., & Le Blanc, F. 2009, *ApJ*, 704, 1262
- Théado, S., Vauclair, S., & Cunha, M. S. 2005, *A&A*, 443, 627
- Turcotte, S. & Charbonneau, P. 1993, *ApJ*, 413, 376
- Turcotte, S., Richer, J., Michaud, G., Iglesias, C. A., & Rogers, F. 1998, *ApJ*, 504, 539
- van den Ancker, M. E., de Winter, D., & Tjin A Djie, H. R. E. 1998, *A&A*, 330, 145
- Vick, M., Michaud, G., Richer, J., & Richard, O. 2010, *A&A*, 521, A62+
- Wade, G. A., Drouin, D., Bagnulo, S., et al. 2005, *A&A*, 442, L31